Research Square

Preprints are preliminary reports that have not undergone peer review.
They should not be considered conclusive, used to inform clinical practice,
or referenced by the media as validated information.

Interrupting Epitaxial Inheritance Through Phase Evolution Enables Grain Refinement in Additive Manufacturing

Atieh Moridi

moridi@cornell.edu

Cornell University

Kaushalendra Singh

Cornell University

Chenxi Tian

Cornell University

Sai Pratyush Akula

Cornell University

Juan Antonio Vega Farje

Cornell University

Amlan Das

Cornell High Energy Synchrotron Source

Batuhan Tak

University of Pittsburgh

Wei Xiong

University of Pittsburgh

Article

Keywords: Additive manufacturing, laser powder bed fusion, PH 17 – 4 stainless steel, microstructure, Operando XRD

Posted Date: November 24th, 2026

DOI: https://doi.org/10.21203/rs.3.rs-11639752/v1

License: This work is licensed under a Creative Commons Attribution 4.0 International License.
Read Full License

Additional Declarations: No competing interests reported.

Interrupting Epitaxial Inheritance Through Phase Evolution Enables Grain Refinement in Additive Manufacturing

Kaushalendra Singh [a], Chenxi Tian [a], Akula Sai Pratyush [a], Juan Antonio Vega Farje [a], Amlan Das [b], Batuhan Tak [c], Wei Xiong [c], Atieh Moridi [a, *]

[a] Sibley School of Mechanical and Aerospace Engineering

Cornell University

124 Hoy Road

Ithaca, NY 14853, USA

[b] Cornell High Energy Synchrotron Source

Cornell University

161 Synchrotron Drive

Ithaca, NY 14853, USA

[c] Department of Mechanical Engineering and Materials Science

University of Pittsburgh

Pittsburgh, PA 15260, USA

*Correspondence to: moridi@cornell.edu

Abstract

The formation of columnar grains through epitaxial growth remains a major challenge in metal additive manufacturing (AM), as the resulting crystallographic texture can contribute to direction-dependent mechanical response, including variations in strength and deformation behavior depending on the loading direction. In this work, we investigate the role of phase evolution pathways in disrupting epitaxial grain propagation during AM of 17-4 PH stainless steel (PH 17-4 SS). Owing to its sensitivity to cooling rate and alloy chemistry, PH 17-4 enables controlled tuning of phase fractions, i.e., ferrite, austenite, and martensite, under different processing conditions. Operando synchrotron X-ray diffraction (XRD) reveals that variations in processing conditions produce different phase evolution behaviors that modify the crystallographic template inherited during subsequent deposition, suppressing

epitaxial grain propagation. Insights gained from operando XRD are then used to fabricate bulk multilayer specimens to tailor microstructural properties such as grain size and crystallographic texture. These findings establish phase evolution as a promising strategy for grain refinement by disrupting epitaxial grain growth in metal AM.

Key words: Additive manufacturing; laser powder bed fusion; PH 17-4 stainless steel; microstructure; Operando XRD

Introduction

Metal additive manufacturing (AM) routinely produces cooling rates that exceed those of conventional casting by several orders of magnitude[1–4]. Classical solidification theory generally predicts that increasing cooling rates promote grain refinement by increasing undercooling and nucleation density[5]. Interestingly, however, coarse columnar grains remain one of the defining microstructural characteristics of metal AM. In AM, grain evolution is governed not only by rapid solidification but also by directional heat flow and crystallographic inheritance during successive deposition cycles. Unlike conventional casting, AM involves repeated cycles of melting, solidification, cooling, reheating, and partial remelting. Consequently, the evolving microstructure is determined not only by the instantaneous solidification conditions but also by the crystallographic template inherited from previously deposited layers. This epitaxial inheritance enables grains to propagate across multiple deposited layers, suppressing the grain refinement that would otherwise be expected from rapid solidification. Consequently, achieving fine equiaxed microstructures requires not only promoting new grain nucleation but also interrupting the continuity of epitaxial grain growth.

Numerous approaches have therefore been developed to suppress columnar grain formation and promote equiaxed grain growth. Modification of solidification parameters, particularly the thermal gradient (G) and solidification growth rate (R), have proven effective in controlling grain morphology. Variations in these parameters have been achieved through modifications to laser scanning strategies [6–8], utilization of multiple laser beams [9–11], implementation of pulsed lasers [12–15], and laser beam shaping [16–18]. The addition of inoculant particles, which can act as nucleation sites in the melt pool, has also been shown to promote grain refinement during metal AM [19–22]. More recently, ultrasound-assisted metal AM has also emerged as a promising technique for grain refinement [23–26]. High-intensity ultrasonic waves generate acoustic cavitation and enhanced melt convection, thereby promoting heterogeneous nucleation and refining the solidification microstructure[26]. Collectively, these approaches modify the conditions at the advancing solidification front by increasing nucleation or altering competitive grain growth. While successful in many alloy

systems, none directly addresses one of the defining characteristics of AM: the repeated epitaxial inheritance that enables grains to propagate across successive deposition cycles.

Tailoring phase evolution pathways offers one possible route to disrupt this crystallographic inheritance. During the rapid thermal cycles characteristic of AM, repeated heating, cooling, and partial remelting continuously modify the crystallographic state of previously deposited material through phase transformations. Because crystallographic inheritance depends on the orientations established during these transformations, altering the sequence and extent of phase evolution may disrupt the transmission of crystallographic orientation across successive deposited layers. Consequently, changes in phase constitution may influence not only the final microstructure but also the crystallographic conditions governing subsequent grain propagation. Despite this possibility, the role of phase evolution in controlling epitaxial inheritance has received little direct experimental attention.

PH 17-4SS provides an ideal model system because relatively small variations in cooling rate and alloy chemistry changes the phase composition significantly. Based on the processing conditions and feedstock powder composition, large variations in the retained austenite fraction (0–97%) have been reported [27–33]. This enables systematic manipulation of phase evolution pathways while maintaining essentially the same alloy system. In this work, we combine operando synchrotron X-ray diffraction (XRD) with post-mortem electron backscatter diffraction (EBSD) to correlate phase evolution with grain evolution during AM of PH17-4SS. To directly probe these effects, we employ operando synchrotron XRD on single-layer prints, to understand how the phase evolution changes with variation in processing conditions. Insights from these single-layer experiments guide the multi-layer printing of samples with tailored grain sizes and crystallographic texture. We further discuss these observations within the framework of epitaxial inheritance and propose that phase evolution provides an effective strategy for reducing epitaxial grain propagation during layer-wise additive manufacturing.

Results

Operando solidification behavior: single layer line scans

The phase evolution during the single-layer line scans can be visualized using heatmaps showing the variation in integrated diffraction intensities in a time vs Q plot (Fig. 1a-1c, top panel). The corresponding bottom panels show the evolution of peak intensities for the most prominent reflections, namely the (110) BCC and (111) FCC peaks, for each processing condition. A corresponding analysis from a repeated scan is provided in Fig. S1, showing that the observed phase evolution is consistent between multiple measurements. Each heatmap reveals three distinct regions of diffraction behavior. The first region corresponds to

diffraction from the feedstock powders. This is followed by signal during heating where the peaks shift toward lower Q values due to thermal expansion, along with a reduction in diffraction intensities as melting initiates. Immediately after melting, solidification occurs and diffraction signals start to reappear. With further cooling, the diffraction peaks progressively shift toward higher Q values as the lattice contracts, continuing until solidification is complete.

The phase evolution during cooling varies with the processing conditions. For samples printed using Argon-atomized (Ar-PH17-4) powder, experiments were performed at scan speeds of 2.5 mm/s and 15 mm/s. The feedstock powder in both cases exhibits primarily BCC diffraction peaks, with weaker peaks corresponding to FCC also present. Immediately after melting, diffraction peaks corresponding to both BCC and FCC phases appear.

At a scan speed of 2.5 mm/s, during the initial stage of cooling, the intensities of both sets of peaks increase until a steady plateau is reached (t = 2.0–2.8 s). As cooling progresses (t > 3.2 s), the FCC peak intensity decreases while the BCC peak intensity increases. This behavior is consistent with the solid-state transformation of FCC austenite to BCT martensite. As the transformation proceeds, the reduction in austenite phase fraction leads to the observed decrease in FCC peak intensity, while martensite formation contributes to the apparent increase in BCC peak intensity. Although the transformation product is BCT martensite, its diffraction peaks closely overlap with those of the BCC phase. As a result, martensite formation manifests as an apparent increase in BCC peak intensity, since the two phases cannot be readily distinguished in the diffraction data.

At the higher scan speed of 15 mm/s, corresponding to a higher cooling rate, the solidification behavior changes. Fig. S2 provides a semi-quantitative estimate of the cooling rates derived from the diffraction data, clearly highlighting the contrast between 2.5 and 15 mm/s scan speeds. Immediately after melting, both BCC and FCC peaks again appear, similar to the lower scan speed case. However, the plateau observed at 2.5 mm/s is absent. Instead, the FCC peak intensity increases transiently (till t=1.6 s) and then decreases without reaching a steady state. The absence of a plateau suggests insufficient time for diffusion-mediated phase transformations to complete. The higher scan speed increases the cooling rate, thereby reducing the time the melt pool remains within the austenite stability temperature range. Consequently, a reduced fraction of austenite and in turn martensite is present in the printed sample.

When the sample is printed using Nitrogen-atomized (N–PH17-4) powders under identical scanning speed (15 mm/s), the phase evolution differs. The intensities of the FCC peaks in the feedstock powder are comparatively higher, consistent with the elevated nitrogen and carbon content introduced during nitrogen atomization, both of which stabilize austenite

and produce a more austenitic starting condition than the Ar-atomized powder. As observed for Ar–PH 17-4 at 15 mm/s, both FCC and BCC peaks appear initially; however, the subsequent decrease in intensity of the FCC peak is much more gradual, indicating a partial transformation of austenite resulting in austenite retention at room temperature.

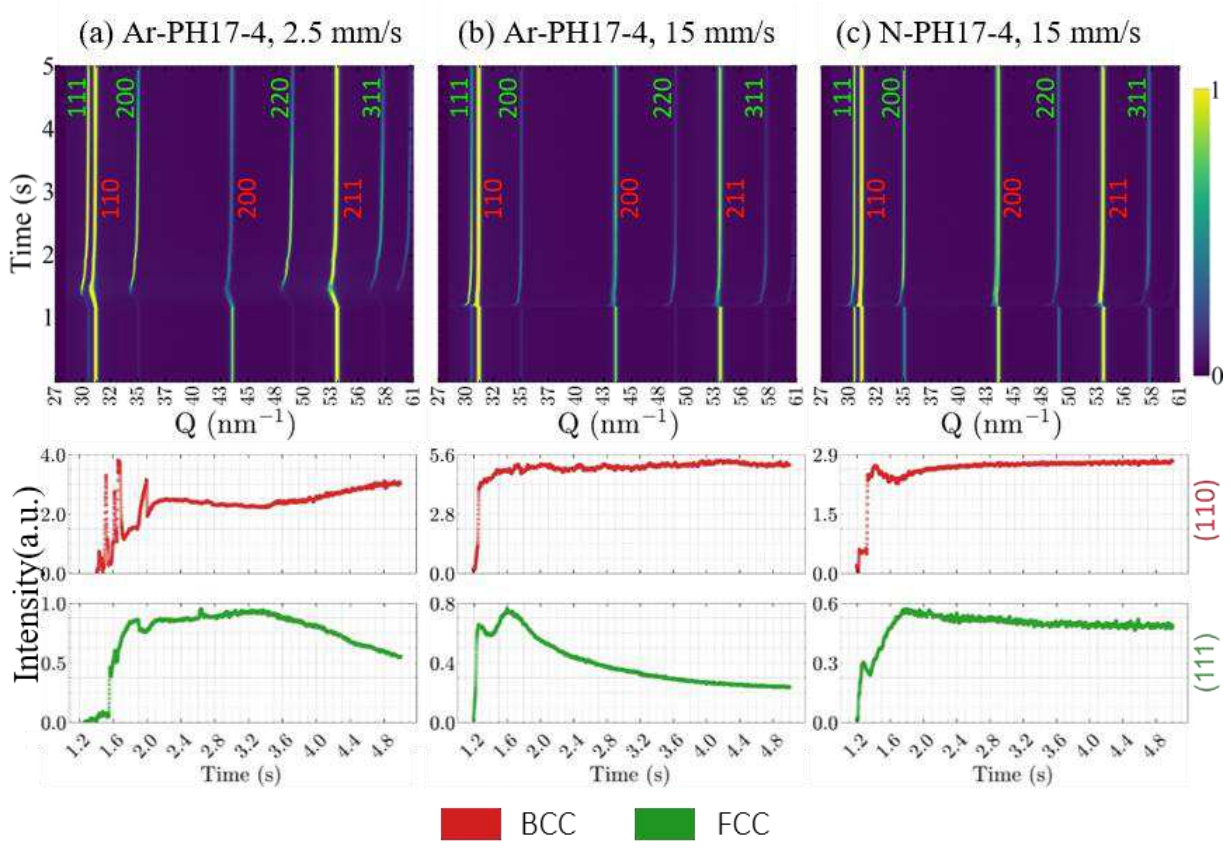


Figure 1 Synchrotron operando XRD showing phase evolution during single line scans at different cooling rates and feedstock composition. *Phase evolution during single-line scans at scan speeds of (a) 2.5, (b) 15 mm/s printed using Ar-PH17-4 powder, and (c) 15 mm/s printed using N-PH17-4 powder, together with the corresponding intensity variation for BCC 110 and FCC 111 reflections.*

Figure 2, which shows phase composition maps for single-layer tracks, directly corroborates the phase evolution observed in the operando XRD data. The top part of each image shows the printed bead, while the bottom section represents the substrate. The X-ray window for the operando experiments was positioned at the intersection of the substrate and powder, such that the captured data provided combined information from both regions. In the bead region, the Ar–PH17-4 samples contain ferrite (red) and martensite (yellow), with martensite primarily located along grain boundaries. The martensite fraction is higher for the slower scan speed of 2.5 mm/s (Fig. 2a) than for 15 mm/s (Fig. 2b). For N–PH17-4 at the higher scan

speed (Fig. 2c), the bead contains substantially larger fractions of both austenite (green) and martensite compared with the Ar–PH17-4 sample. Similar trends are observed in the substrate, although the magnitude of the phase changes differs from that in the bead. The substrate is reheated by the passing laser, raising its temperature into the austenite range and promoting martensite formation from the grain boundaries upon subsequent cooling. Accordingly, the substrate martensite fraction is highest at the slower scan speed of 2.5 mm/s and lowest at 15 mm/s, consistent with the increased thermal exposure at lower scan speeds. The phase distribution for each sample, combining both bead and substrate regions, is summarized in Table 1. Overall, the Ar–PH 17-4 samples exhibit predominantly two-phase ferrite–martensite microstructures, with a higher martensite fraction at 2.5 mm/s (15–36%) than at 15 mm/s (5–14%), while austenite remains below 1% in both conditions. In contrast, the N–PH 17-4 sample exhibits a three-phase microstructure, consisting of 39–62% ferrite, 11–45% martensite, and 16–25% austenite.

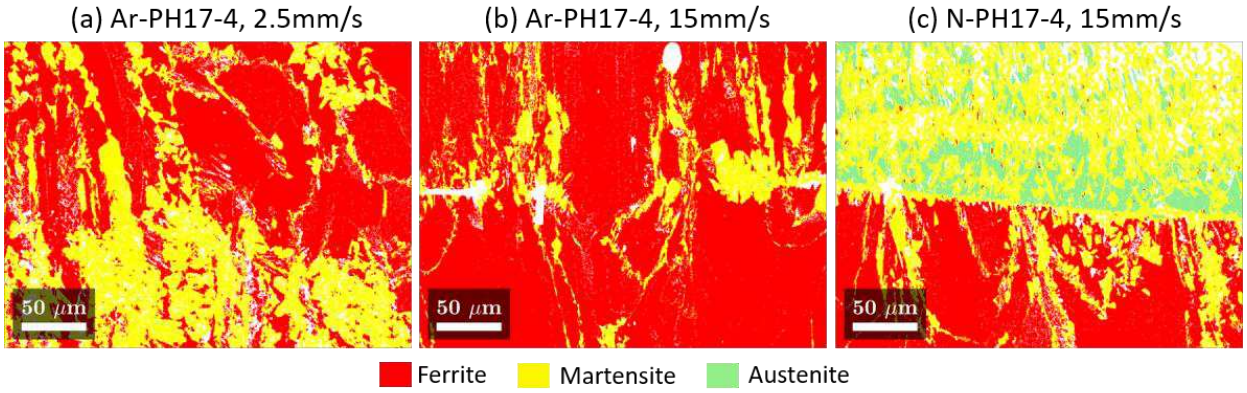


Figure 2 Phase distribution in single-line tracks corroborates the operando phase evolution. *Phase composition maps for single-layer (a) Ar-PH 17-4 sample at low cooling rate, (b) high cooling rate, and (c) N-PH17-4 sample at high cooling rate. Red denotes ferrite, green denotes austenite, yellow denotes martensite, and white corresponds to unindexed regions*

Powder	Scan speed(mm/s)	Ferrite (%)	Martensite (%)	Austenite (%)
Ar-PH17-4	2.5	63-85	15-36	<1
Ar-PH17-4	15	86-94	5-14	< 1
N-PH17-4	15	39-62	11-45	16-25

Table 1 Phase composition of samples from single layer operando XRD experiments

Through a combination of operando and post-mortem characterization, we demonstrate that phase evolution pathways in AM PH 17-4 SS are highly sensitive to processing conditions and feedstock composition. Operando XRD measurements reveal that even

modest changes in cooling rate, achieved by varying the scan speed and the feedstock composition, lead to measurable deviations from equilibrium behavior which manifested as changes in phase composition of the printed samples. However, the extent to which the phase evolution pathway can be altered is likely greater than what is captured within the limited cooling rate range explored here.

During the operando XRD experiments, the cooling rates could only be varied by approximately one order of magnitude, as further variation was limited by signal quality. We anticipate that extending this range would lead to more pronounced deviations from equilibrium solidification behavior. At sufficiently high cooling rates, complete austenite bypass may occur, a phenomenon previously reported in PH 17-4 SS[34]. In this scenario, the phase evolution pathway would proceed entirely through the ferritic phase, resulting in more pronounced variations in both phase composition and microstructure.

To access a broader range of cooling rates beyond these experimental limitations, we compared samples processed using DED and PBF. In general, PBF achieves cooling rates approximately two orders of magnitude higher than those in DED [2], providing a useful framework to investigate the effects of substantially increased cooling rates on phase evolution. As both DED and PBF are widely used metal AM production processes, this comparison also reveals how the phase evolution trends identified in the single-line operando experiments extend to production-relevant, multilayer builds.

Comparing DED vs PBF

Following the trends identified in operando single-line scans, multilayer samples were fabricated using DED and PBF to evaluate the extent to which phase evolution pathways can be altered. Post-mortem EBSD characterization (Fig. 3a) shows that the multilayer samples follow the same trends observed in the operando experiments, but with significantly amplified effects due to the larger variation in cooling rates. The phase compositions of the multilayer samples are also summarized in Table 2.

The Ar-DED multilayer samples exhibit a dual-phase microstructure consisting of ferrite (53 61%) and martensite (38-46%) distributed throughout the sample. In contrast, the Ar-PBF samples are predominantly ferritic (95-99%), with only a small fraction of martensite (0-4%) localized along grain boundaries. This marked shift confirms that large variation in the cooling rate can drive the system toward a fundamentally different phase evolution pathway. In comparison, the N-PBF samples exhibit a three-phase microstructure comprising of ferrite (26-31%), martensite (48-55%), and austenite (17-21%). Consistent with the operando results, the use of N–PH 17-4 powders enabled the reintroduction of martensite along with retention of austenite, even under the high cooling rates of PBF.

Samples	Ferrite (%)	Martensite (%)	Austenite (%)	Solidification mode
Ar-DED	53-61	38-46	<1	Mixed mode
Ar-PBF	95-99	0-4	< 1	Single phase
N-PBF	26-31	48-55	17-21	Mixed mode

Table 2 Phase composition of samples printed under DED and PBF

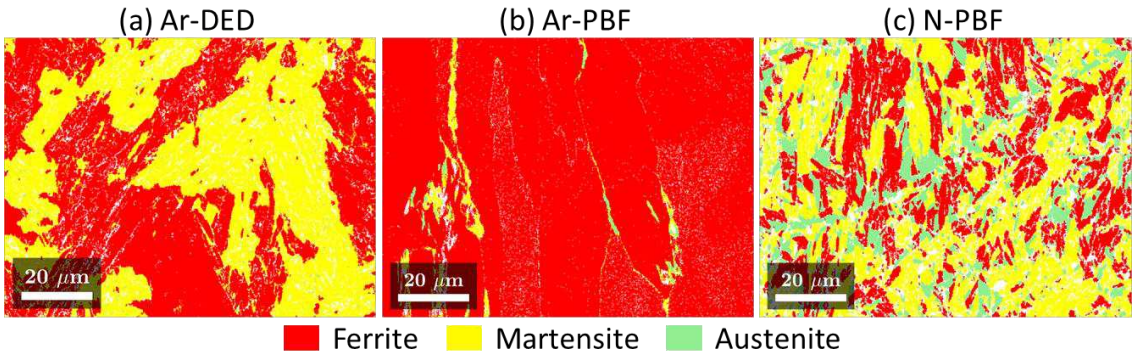


Figure 3 Phase distribution in multilayer DED and PBF builds. *EBSD Phase maps for (a) Ar-DED, (b) Ar-PBF and (c) N-PBF samples. Red denotes ferrite, green denotes austenite, yellow denotes martensite, and white corresponds to unindexed regions*.

Quantitative grain size analysis reveals a result that contrasts with conventional expectations in metal AM, where PBF typically produces finer grains than DED for the same material system. The area-weighted mean grain size of the Ar-DED sample (22.12 μm) is approximately four times smaller than that of the Ar-PBF sample (93.41 μm) - the opposite of the typical trend. The N-PBF sample, however, exhibits the smallest average grain size of all (5.93 μm), showing that feedstock modification restored the expected grain-refining effect of PBF's higher cooling rates. Grain size distribution maps obtained from large-area EBSD scans (Fig. 4), illustrate these trends spatially. The statistics of grain size distribution are summarized in Table 3, and the corresponding histograms are shown in Fig. S3.

Sample	Area-weighted Mean (μm)	D10 (μm)	D90 (μm)
Ar-DED	22.12	3.28	57.27
Ar-PBF	93.41	33.87	146.66
N-PBF	5.93	1.87	11.66

Table 3 Grain size statistics for Ar-DED, Ar-PBF and N-PBF samples

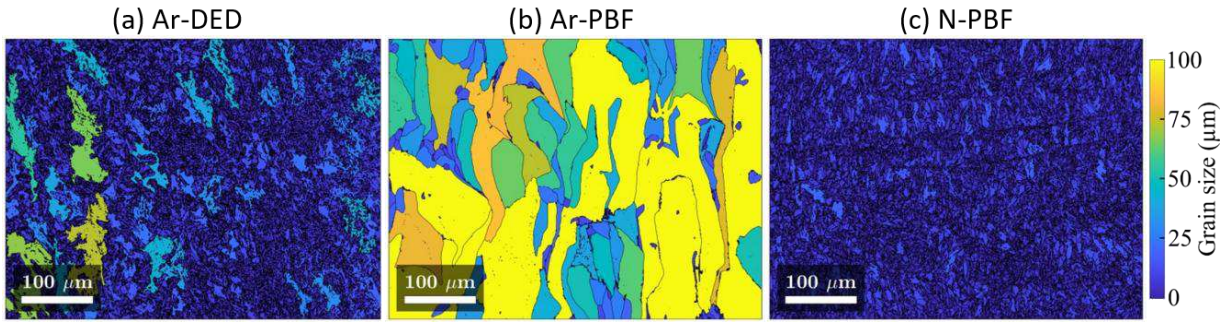


Figure 4 Grain size distribution in multilayer DED and PBF builds. *Grain size maps from large-area EBSD scans of (a) Ar-DED, (b) Ar-PBF and (c) N-PBF samples, colored by equivalent grain diameter.*

Beyond grain size, the orientation and crystallographic texture also varied across the different conditions. The IPF maps and associated {100} pole figures for the BCC phase (encompassing both ferrite and martensite) illustrate this effect. The Ar-DED sample (Fig. 5a) exhibits relatively weak texture (Texture Index, TI = 1.50). In contrast, the Ar-PBF sample (Fig. 5b) develops a strong texture with grains largely aligned parallel to the build direction, as reflected in a high TI of 4.95. Finally, in the N-PBF sample (Fig. 5c), the texture is again weakened, resulting in a more randomized grain orientation with the TI reduced to 1.13.

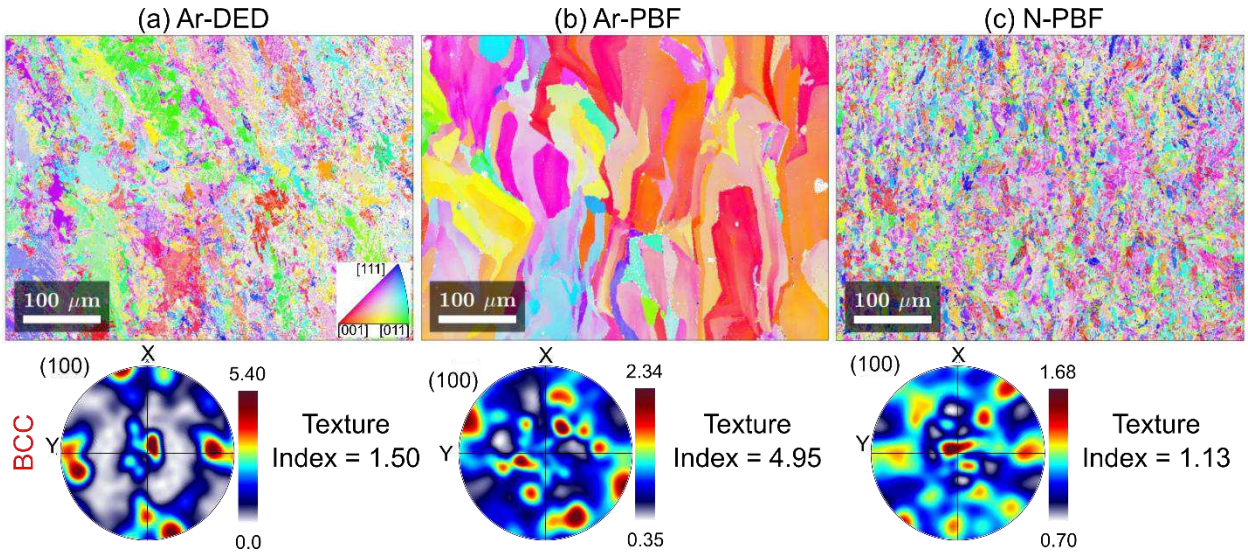


Figure 5 Crystallographic texture of the BCC phase in multilayer builds. *IPF-Z maps and {100} pole figures of the BCC phase (ferrite and martensite) for (a) Ar-DED, (b) Ar-PBF and (c) N-PBF samples, with Z parallel to the build direction.*

Taken together, these results demonstrate that while operando experiments captured the sensitivity of phase evolution to processing conditions, the use of a wider processing window revealed the full extent of this control. Specifically, the solidification pathway can be shifted

from a *mixed-mode* (Ar–DED) to a predominantly *single-phase* (Ar–PBF), and further tuned back to a *mixed-mode* through feedstock modification (N–PBF). This control over phase evolution directly governs the resulting grain size and texture. The Ar-DED and N-PBF conditions, both undergoing mixed-mode solidification, produce finer, more equiaxed grains and weaker texture, while the single-phase Ar-PBF condition produces coarse columnar grains and strong build-direction texture.

Discussion

The differences in solidification behavior, and consequently the resulting microstructures, arise from the interplay between thermodynamic phase stability and the kinetics of phase transformation in PH17-4 SS. The operando synchrotron XRD experiments establish that relatively modest changes in processing conditions and feedstock compositions introduce variations in the phase evolution pathways. Increasing cooling rate suppresses the diffusion-controlled ferrite-to-austenite transformation, while increasing the thermodynamic stability of austenite restores significant FCC formation even under higher cooling rates. This variation in phase evolution pathways is further amplified when comparing DED and PBF, owing to the substantially wider range of cooling rates accessible between these two processes relative to the single-line experiments. Across this wider range, the resulting phase evolution pathways diverge considerably between the two processes - from predominantly single-phase ferritic solidification in Ar-PBF to a mixed-mode solidification in Ar-DED. Notably, despite the high cooling rates inherent to PBF - which would otherwise suppress ferrite-to-austenite transformation - a mixed-mode phase evolution pathway was recovered by modifying the feedstock composition (N-PBF). This divergence in phase evolution pathway directly governs the resulting grain size and texture in the multilayer builds, as reflected in the contrasting microstructures observed across the Ar-DED, Ar-PBF, and N-PBF conditions.

A schematic illustrating the proposed grain evolution mechanisms for all three processing conditions, compared to conventional manufacturing like casting, is shown in Fig. 6. In the case of casting, solidification begins with heterogeneous nucleation of ferritic grains at the mold walls (Fig.6a). These nuclei subsequently grow into the undercooled liquid as cooling proceeds, with relatively few nucleation events allowing the initially formed grains to grow extensively before solidification is complete. Consequently, conventional casting produces a relatively coarse-grained microstructure. Under the near-equilibrium conditions achieved during casting, the ferrite then undergoes a complete diffusion-driven transformation to austenite. The solidified alloy is subsequently rapidly quenched to obtain the hardened martensitic phase through a displacive transformation.

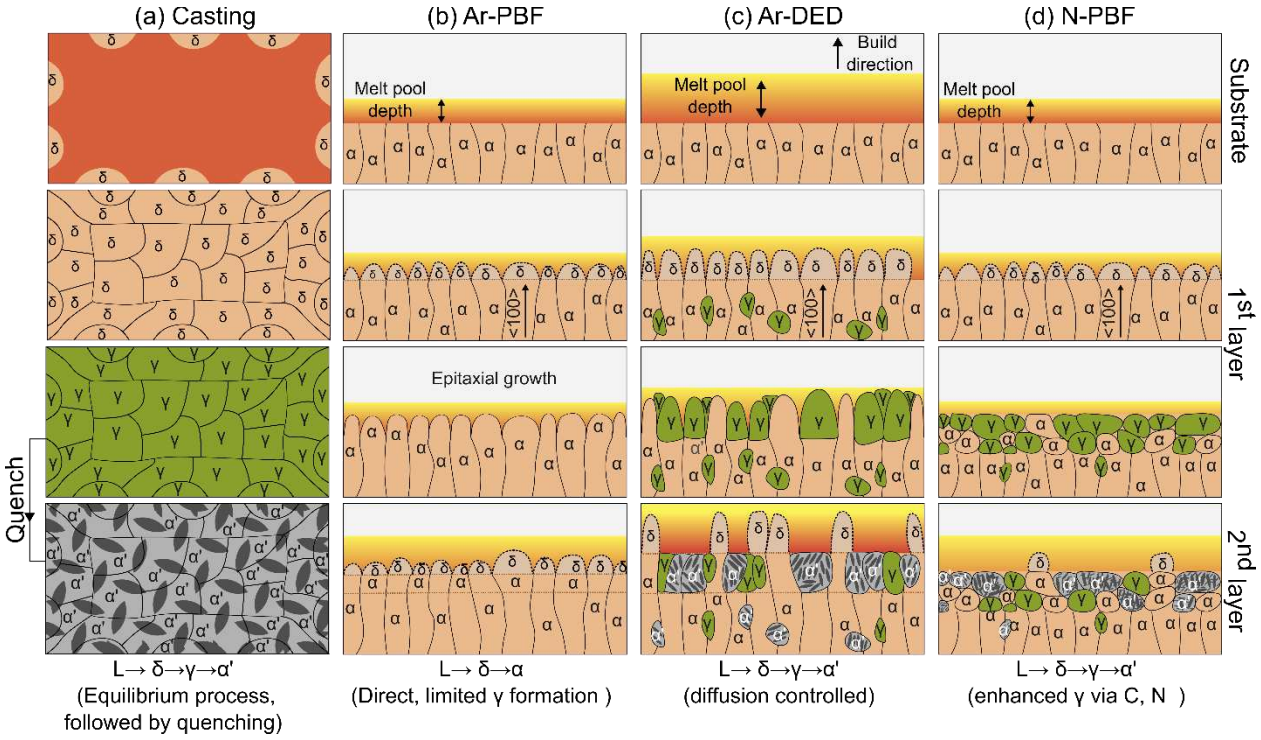


Figure 6 Proposed phase evolution and grain growth mechanisms in casting and AM. *Schematic of phase evolution (α – Ferrite, γ- Austenite, α'-Martensite) evolution and multilayer grain growth behavior during (a) Casting, (b) Ar-PBF, (c) Ar-DED, and (d) N-PBF conditions*

In the case of the Ar-PBF sample (Fig. 6b), solidification proceeds predominantly through a single-phase ferritic solidification. Cubic crystal structures (BCC and FCC) exhibit preferred growth along the ⟨100⟩ crystallographic direction under directional solidification conditions [35–37]. Since ferrite is the primary solidifying phase, its crystal structure matches that of the substrate layer. As a result, the BCC ferritic grains with their <100> direction aligned with the thermal gradient can undergo epitaxial growth, which has no activation barrier [38,39] - leading to the formation of columnar grains. Under equilibrium conditions, these ferritic grains are expected to fully transform into austenite. However, the high cooling rates associated with PBF suppress the diffusion-driven ferrite-to-austenite transformation. Consequently, only limited amounts of austenite form, preferentially along grain boundaries where diffusion is enhanced[40], while the majority of the ferritic microstructure remains unchanged. During deposition of subsequent layers, partial remelting of the underlying material occurs. Because the surviving BCC grains retain their crystallographic orientation, they continue to act as epitaxial templates for the newly solidifying ferrite. Repetition of this process over successive layers results in the development of large columnar grains that extend across multiple melt pool boundaries (Fig. 7a) and produce the strong build-direction texture observed experimentally.

For the same Ar-PH17-4 powder, a mixed-mode solidification pathway is observed in the Ar-DED sample (Fig. 6c). Compared with Ar-PBF, the Ar-DED microstructure contains substantially higher fractions of austenite and martensite. This difference arises primarily from the relatively lower cooling rates in DED, which provide sufficient time for diffusion-controlled ferrite-to-austenite transformation following primary ferritic solidification. Similar to the Ar-PBF condition, solidification initially begins with epitaxial growth of BCC ferrite. However, the slower cooling permits a significant fraction of the ferrite to transform into austenite, which subsequently transforms into martensite during further cooling. As a result, unlike the Ar-PBF condition, the first deposited layer consists of a mixture of ferrite, austenite, and martensite.

During deposition of subsequent layers, the partially remelted region therefore contains BCC ferrite, FCC austenite, and BCT martensite. While BCC seed grains can still facilitate epitaxial growth of the BCC phase, epitaxial growth is unlikely to proceed from FCC or BCT phases due to crystallographic mismatch[41]. In regions where suitable BCC templates are absent, solidification proceeds through heterogeneous nucleation of ferrite rather than epitaxial growth. Compared to epitaxial growth, nucleation-driven growth promotes grain refinement and disrupts the strong texture typically associated with epitaxial solidification. Consequently, the grains remain confined between two melt pool boundaries rather than extending across multiple melt pools (Fig. 7b). Furthermore, repeated thermal cycling during deposition of subsequent layers promotes additional solid-state ferrite-to-austenite transformation, further increasing the fractions of transformed phases throughout the build.

The kinetic feasibility of the diffusion-controlled ferrite-to-austenite transformation can be evaluated by comparing the characteristic diffusion length of the fast-diffusing interstitial species(C,N) with the measured Primary Dendrite Arm Spacing (PDAS). Since Ar-PH17-4 powder contains no measurable N, only C diffusion is considered for this composition. For the Ar-PBF condition, the calculated diffusion length (0.13–0.30 μm) is smaller than the measured PDAS (0.38 ± 0.1 μm), giving an L/PDAS ratio of 0.5–0.6, indicating that carbon redistribution across the dendritic spacing is kinetically restricted and supporting the near-complete suppression of the diffusion-controlled transformation. In contrast, for the Ar-DED condition, the calculated C diffusion length (0.80–1.72 μm) is comparable to the measured PDAS (1.22 ± 0.3 μm), giving an L/PDAS ratio of 0.9–1.1 across the measured range, indicating that diffusion over the dendritic length scale is feasible within the available solidification time and is consistent with the substantial phase transformation described above.

Interestingly, even at the high cooling rates in PBF, the solidification can be shifted from predominantly ferritic to mixed-mode solidification by increasing the thermodynamic stability of the austenite phase through the use of N-PH17-4 powder (Fig. 6d). The higher

concentrations of the strong austenite stabilizers, C and N, increase the thermodynamic stability of the FCC phase, thereby promoting the formation and retention of austenite even under rapid solidification conditions. Consequently, the N-PBF sample exhibits a mixed-mode solidification behavior similar to that observed in the Ar-DED condition. Solidification initially proceeds through epitaxial growth of BCC ferrite from the underlying layer. However, because the PBF melt pool is substantially smaller than that in DED, the initial epitaxially grown ferrite grains are correspondingly finer, producing smaller transformed austenite grains that subsequently form martensite during cooling. The increased thermodynamic stability of austenite also enables partial retention of the FCC phase at room temperature.

During deposition of subsequent layers, the remelted region again consists of a mixture of BCC ferrite, FCC austenite, and BCT martensite. Although epitaxial growth remains possible from the surviving BCC ferrite, its contribution is reduced because of both the finer grain size and the lower fraction of available BCC seed grains following phase transformation. Consequently, heterogeneous nucleation becomes the dominant mechanism governing grain formation during subsequent solidification. Post-mortem characterization confirms that grains do not propagate across melt pool boundaries (Fig. 7c), indicating that grain growth is repeatedly interrupted. Combined with the smaller melt pools in N-PBF, which further limit grain growth, this results in finer grains than those observed under the mixed-mode solidification conditions in Ar-DED.

A limitation of the present study is that our observations do not distinguish whether reduced epitaxial persistence is the initiating mechanism for grain refinement or a consequence of different phase evolution pathways. Nevertheless, grain refinement is consistently accompanied by reduced epitaxial growth across successive deposition cycles, supporting the robustness of this relationship despite the unresolved causal mechanism. A further limitation is that differences between PBF and DED are primarily attributed to cooling rate, although other process-dependent factors may also contribute. However, the consistent trends observed between the N- and Ar-atomized powders under otherwise comparable PBF conditions provide supporting evidence for the proposed interpretation.

Overall, these results demonstrate that grain evolution in AM PH17-4 SS is governed by the coupled effects of thermodynamic phase stability and transformation kinetics. Rapid cooling in Ar-PBF suppresses diffusion-controlled phase transformation, preserving uninterrupted epitaxial ferrite growth, whereas the lower cooling rates in Ar-DED and enhanced austenite stability in N-PH17-4 promote mixed-phase microstructures that interrupt epitaxial growth and increase heterogeneous nucleation. The balance between these competing mechanisms ultimately determines the grain morphology, phase distribution, and crystallographic texture.

More broadly, in alloy systems where primary solidification proceeds through a single phase that transforms substantially before the next deposition cycle - with epitaxial growth otherwise dominating - manipulating phase evolution pathways offers an effective strategy for interrupting epitaxial grain inheritance and controlling the resulting microstructure.

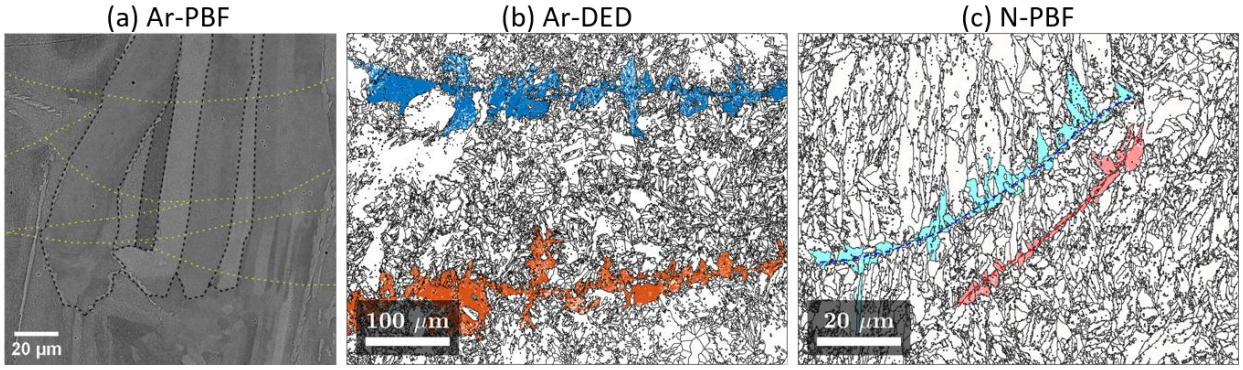


Figure 7 Grain continuity across melt- pool boundaries in multilayer builds. *(a) SEM image of the Ar-PBF sample showing large columnar grains (outlined in black) crossing multiple melt pool boundaries (outlined in yellow). EBSD maps of the (b) Ar-DED and (c) N-PBF samples, with grains colored to match their containing melt pool boundary, showing that grains do not cross melt pool boundaries.*

Methods

Materials

Two sets of PH 17-4SS powders-one atomized in an argon atmosphere (Ar-PH17-4) and the other in a nitrogen atmosphere (N-PH17-4) -were procured from Carpenter Additive. The same sets of powders were used for fabrication in both PBF and DED processes to enable direct comparison. The nominal composition of both powder sets as provided by the supplier are shown in Table 4. Powder XRD measurements were performed using a Bruker D8 Advance ECO diffractometer to characterize both powder feedstocks (Fig. S4). The XRD results highlight clear differences in phase composition between the two powders: Ar–PH17-4 is predominantly ferritic, whereas N–PH17-4 contains a significantly high fraction of the austenite phase.

Powder	C	N	Mo	Cu	Nb	Ni	Cr	Si	Mn	Fe
Ar-PH17-4	0.02	-	0.01	3.31	0.28	4.38	15.76	0.41	0.39	balance
N-PH17-4	0.05	0.09	0.05	3.17	0.26	3.35	15.45	0.64	0.30	balance

Table 4 Elemental compositions (wt. %) of PH 17-4 SS powders

Operando XRD synchrotron

Operando XRD experiments were conducted at the Forming and Shaping Technology (FAST) ID3A beamline at the Cornell High Energy Synchrotron Source (CHESS). Single-layer line scans were performed using a custom-AM setup[42–44] developed in our lab and integrated directly at the beamline. A 500 W multi-mode IPG laser (YLR-500-MM, spot size = 450 μm), operating at a wavelength of 1064 nm was integrated with a scan head (Cambridge Tech ProSeries II) to fabricate the line prints. The operando solidification behavior was investigated by continuously capturing diffraction patterns during the printing process. A 100 × 100 μm high-energy X-ray beam with an energy of 61.332 keV and an energy bandwidth of 5×10^{-3} keV, generated using a multilayer (alternating W/B_4C layers) monochromator, was positioned at the powder-substrate interface to probe phase evolution during printing. Time-resolved diffraction patterns were captured in transmission mode using a CdTe Eiger 500K (512 × 1024 pixels) area detector operating at a frame rate of 1 kHz. The detector-to-sample distance, calibrated using CeO_2 powder, was optimized at 690 mm to capture maximum number of diffraction peaks while maintaining adequate peak separation.

Single layer line prints

To understand the changes in phase evolution of PH 17-4 SS during XRD analysis, XRD data were collected during the printing of single line scans under different processing conditions. The effect of cooling rate on phase evolution was studied by increasing the scan speed from 2.5 mm/s to 15 mm/s. The effect of powder composition was investigated by using N-PH17-4 powder for a line scan printed at 15 mm/s. For all experiments, the substrate was machined directly from PBF-printed PH 17-4 SS fabricated with Ar-PH17-4 powder to eliminate substrate-related effects. The details of the different line scans are shown in Table 5.

Powder	Laser Power (W)	Scan speed (mm/s)
Ar-PH17-4	100	2.5
Ar-PH17-4	100	15
N-PH17-4	100	15

Table 5 Experimental details of different single-layer prints

Multilayer prints

Multilayer DED samples were printed using a FormAlloy X2 DED system equipped with an IPG Photonics Nd:YAG continuous wave fiber laser, operating at a maximum power of 500W and a spot size of 1.2 mm. The multilayer DED samples were printed at a laser power of 325

W, with laser scanning speed of 800 mm/min with a layer height of 0.2 mm and hatch spacing of 0.6mm. The multilayer PBF samples were fabricated using an SLM280 Twin Laser machine with a layer thickness of 40 µm, at a volumetric energy density of 66.7 J/mm^3. The multilayer DED samples (hereafter referred to as Ar-DED) were printed using Ar-PH17-4 powders, while the PBF samples were printed using both Ar-PH17-4 (hereafter Ar-PBF) and N-PH17-4 powders (hereafter N-PBF).

XRD data analysis

The time versus scattering vector (Q) heat maps showing the phase evolution were generated by integrating the raw 2D detector images radially along the observed azimuthal range (257-290^o) using the GSAS-II software [45]. Each detector frame was integrated with 2500 bins in a Q range of 27-61 nm^{-1}. The peak positions and peak intensities were determined by fitting a pseudo-voigt function for each peak in every frame. The intensity ratio vs. time plots for each peak were generated by tracking the fitted peak intensity across all frames.

Microstructural characterization

Post-mortem characterization of the multilayer prints and single-line scans was conducted by evaluating the microstructure in cross-sections perpendicular to the laser-scan direction. The sectioned surfaces were first prepared using standard polishing procedures, polishing up to 0.08 µm with colloidal SiC, and then electropolished in a 5 vol.% perchloric acid and ethanol mixture. Microstructure and phase composition were assessed using a Zeiss Gemini 500 scanning electron microscope (SEM) equipped with a QUANTAX electron backscatter diffraction (EBSD) system. The EBSD maps for the single layer prints were collected from the region probed during the x-ray experiments. For the bulk multilayer samples, two sets of EBSD data were collected: one at a smaller view field (100 µm) and another at a larger view field (500 µm). The step size for all EBSD maps acquired at the smaller view field was 0.20 µm, whereas the step size for the larger view field maps was optimized to achieve an acquisition time of approximately 1 hour. The phase composition maps were obtained using the smaller view field maps whereas the larger view field maps were used to determine the grain size distributions. The EBSD data was analyzed using the open-source MTEX software[46]. Grain sizes were quantified using the equivalent circle diameter (ECD), defined from the area of each grain. Average grain size for each condition was calculated using an area-weighted approach.

Differentiation of Ferrite and Martensite

Because the lattice parameters of BCC ferrite and BCT martensite are very similar, EBSD phase indexing alone cannot reliably distinguish between the two phases, and both phases are initially indexed as BCC. Martensite forms through the rapid shear distortion of FCC

austenite into the BCT structure. This transformation is accompanied by both a volume expansion and a shape change, generating significant local lattice distortion and high dislocation density[47–49]. Consequently, martensitic regions exhibit degraded diffraction pattern quality and higher local misorientations compared to ferrite[50,51]. Exploiting these differences, a combination of band contrast (BC) and kernel average misorientation (KAM) was used to differentiate martensite from ferrite. BC quantifies the diffraction pattern quality, while KAM measures the local lattice misorientation around each pixel by averaging the misorientation between that pixel and its neighboring pixels. Martensitic regions therefore appear as areas of low BC[52] and high KAM[50,53], whereas ferritic regions show high BC and low KAM. Threshold values for BC and KAM were then determined from the distributions of grain-averaged values across each EBSD map. Grains with BC below the BC threshold and KAM above the KAM threshold were then classified as martensite, while grains above the BC threshold and below the KAM threshold were classified as ferrite. The grain-averaged BC and KAM maps used for thresholding in the operando and multilayer experiments are shown in Figs. S5 and S6.

Kinetics Feasibility

To evaluate the kinetic feasibility of the equilibrium δ-ferrite-to-austenite transformation under the rapid cooling conditions encountered during AM, the calculated diffusion lengths of the primary fast diffusing species (C and N) were compared with the PDAS, which serves as the characteristic diffusion length scale for solute redistribution during the transformation. Interdiffusion coefficients, D(T), for C and N in the Ar-PH17-4 and N-PH17-4 compositions were calculated using DICTRA with the TCFE13 thermodynamic and MOBFE8 mobility databases, at 1100–1400 °C (Table S1). D(T) was fit to an exponential function, $D(T)= D_o \exp(-k/T)$, and integrated over the equilibrium δ-ferrite-to-austenite transformation window, with the onset and completion temperatures determined from equilibrium phase fraction diagrams (Fig. S7) calculated using Thermo-Calc: 1250–1437°C for Ar-PH17-4. The diffusion length was then computed as $L = \sqrt{(\int D(T)dT/CR)}$.Local cooling rates were estimated from measured PDAS via $\lambda = \alpha \cdot CR^{-0.33}$ ($\alpha = 80$) [54] . The PDAS values, measured from SEM images of etched samples, were measured to be 1.22 ± 0.3 μm and 0.38 ± 0.1 μm for the Ar-DED and Ar-PBF samples (Fig. S8), respectively, giving cooling rates of approximately 3.2×10^5 K/s (range: 1.6–7.5 × 10^5 K/s) and 1.1×10^7 K/s (range: 5.4×10^6–2.8×10^7 K/s)

Data and materials availability

The datasets generated during and/or analyzed during the current study are available from the corresponding author on reasonable request.

CRediT authorship contribution statement

Kaushalendra K Singh: Investigation, Writing – review & editing, Methodology, Data curation. **Chenxi Tian:** Writing – review & editing, Methodology, Data curation. **Amlan Das:** Writing – review & editing, Methodology, Data curation. **Akula Sai Pratyush:** Writing – review & editing, Methodology, Data curation. **Juan Antonio Vega**: Writing – review & editing, Methodology, Data curation. **Batuhan Tak:** Formal analysis, Writing – review & editing, Data curation. **Wei Xiong:** Formal analysis, Software, Writing – review & editing. **Atieh Moridi:** Conceptualization, Writing – review & editing.

Declaration of Competing Interest

The authors declare that they have no known competing financial interests or personal relationships that could have appeared to influence the work reported in this paper.

Acknowledgements

This work is primarily supported by the U.S. Department of Energy, Office of Science, Basic Energy Sciences Early Career Award (DE-SC0022860). The design of the setup for operando experiments is supported by the National Science Foundation CAREER Award (CMMI-2046523). This work is based upon research conducted at the Center for High Energy X-ray Sciences (CHEXS), which is supported by the National Science Foundation (BIO, ENG and MPS Directorates) under award (DMR-1829070). Wei Xiong acknowledges funding from the National Science Foundation CAREER Award (CMMI 2047218). The authors acknowledge the contributions of Katherine Shanks during operando experiments and data analysis. The authors also acknowledge Moog Inc. for supplying the powders and printing the PBF samples.

5.References

1. Manvatkar, V., De, A. & DebRoy, T. Heat transfer and material flow during laser assisted multi-layer additive manufacturing. *J. Appl. Phys.* **116**, 124905 (2014).
2. DebRoy, T. *et al.* Additive manufacturing of metallic components – Process, structure and properties. *Progress in Materials Science* **92**, 112–224 (2018).

3. Li, Y. & Gu, D. Parametric analysis of thermal behavior during selective laser melting additive manufacturing of aluminum alloy powder. *Materials & Design* **63**, 856–867 (2014).
4. Kistler, N. A., Nassar, A. R., Reutzel, E. W., Corbin, D. J. & Beese, A. M. Effect of directed energy deposition processing parameters on laser deposited Inconel® 718: Microstructure, fusion zone morphology, and hardness. *J. Laser Appl.* **29**, 022005 (2017).
5. Prasad, A. *et al.* Towards understanding grain nucleation under Additive Manufacturing solidification conditions. *Acta Materialia* **195**, 392–403 (2020).
6. Arısoy, Y. M. *et al.* Influence of scan strategy and process parameters on microstructure and its optimization in additively manufactured nickel alloy 625 via laser powder bed fusion. *Int J Adv Manuf Technol* **90**, 10.1007/s00170-016-9429-z (2017).
7. Wan, H. Y., Zhou, Z. J., Li, C. P., Chen, G. F. & Zhang, G. P. Effect of scanning strategy on grain structure and crystallographic texture of Inconel 718 processed by selective laser melting. *Journal of Materials Science & Technology* **34**, 1799–1804 (2018).
8. Raghavan, N. *et al.* Localized melt-scan strategy for site specific control of grain size and primary dendrite arm spacing in electron beam additive manufacturing. *Acta Materialia* **140**, 375–387 (2017).
9. Attariani, H., Petitjean, S. R. & Niekamp, A. M. Synchronized Multi-Laser Powder Bed Fusion (M-LPBF) Additive Manufacturing: A Technique for Controlling the

Microstructure of Ti–6Al–4V. *Journal of Manufacturing and Materials Processing* **8**, 242 (2024).

10. Bergmueller, S., Scheiber, J., Kaserer, L. & Leichtfried, G. Enhancing equiaxed grain formation in a high-alloy tool steel using dual laser powder bed fusion. *Additive Manufacturing* **74**, 103727 (2023).
11. Liu, Z. *et al.* Effect of dual-laser powder bed fusion on surface quality, internal defects and properties of 316L stainless steel. *Journal of Materials Research and Technology* **27**, 5681–5691 (2023).
12. Karna, S. *et al.* On the microstructure evolution of AA6061 with pulsed laser powder bed fusion. *Materials Research Letters* **13**, 439–447 (2025).
13. Ma, L. *et al.* Influence of pulsed laser scanning patterns on microstructural evolution and mechanical properties of Inconel 718 in direct laser deposition. *Journal of Materials Research and Technology* **25**, 1231–1244 (2023).
14. Yoon, H. *et al.* Pulsed laser-assisted additive manufacturing of Ti-6Al-4V for in-situ grain refinement. *Sci Rep* **12**, 22247 (2022).
15. Chen, H. *et al.* Effects of pulsed frequency on the microstructure characteristics and properties of Ti6Al4Vlaser melting deposition additive manufacturing parts. *Journal of Materials Research and Technology* **28**, 53–65 (2024).
16. Shi, R. *et al.* Microstructural control in metal laser powder bed fusion additive manufacturing using laser beam shaping strategy. *Acta Materialia* **184**, 284–305 (2020).

17. Tumkur, T. U. *et al.* Nondiffractive beam shaping for enhanced optothermal control in metal additive manufacturing. *Science Advances* **7**, eabg9358 (2021).
18. Roehling, T. T. *et al.* Controlling grain nucleation and morphology by laser beam shaping in metal additive manufacturing. *Materials & Design* **195**, 109071 (2020).
19. Tan, Q. *et al.* A novel method to 3D-print fine-grained AlSi10Mg alloy with isotropic properties *via* inoculation with LaB6 nanoparticles. *Additive Manufacturing* **32**, 101034 (2020).
20. Zhai, W., Zhu, Z., Zhou, W., Nai, S. M. L. & Wei, J. Selective laser melting of dispersed TiC particles strengthened 316L stainless steel. *Composites Part B: Engineering* **199**, 108291 (2020).
21. Mantri, S. A. *et al.* The effect of boron on the grain size and texture in additively manufactured β-Ti alloys. *J Mater Sci* **52**, 12455–12466 (2017).
22. Bermingham, M., StJohn, D., Easton, M., Yuan, L. & Dargusch, M. Revealing the Mechanisms of Grain Nucleation and Formation During Additive Manufacturing. *JOM* **72**, 1065–1073 (2020).
23. Zhang, M. *et al.* Grain refinement of NiTi alloys during ultrasound-assisted wire-arc directed energy deposition. *Virtual and Physical Prototyping* **19**, e2289465 (2024).
24. Ji, F. *et al.* Grain refinement and mechanism of steel in ultrasound assisted wire and arc additive manufacturing. *International Communications in Heat and Mass Transfer* **143**, 106724 (2023).
25. Heidowitzsch, M. *et al.* Grain size manipulation by wire laser direct energy deposition of 316L with ultrasonic assistance. *Journal of Laser Applications* **35**, 032017 (2023).

26. Todaro, C. J. *et al.* Grain structure control during metal 3D printing by high-intensity ultrasound. *Nat Commun* **11**, 142 (2020).
27. Singh, K. K. & Moridi, A. Metastability mediated grain size control in PH 17-4 stainless steel fabricated using Laser-Powder Bed Fusion (LPBF). *Materialia* **30**, 101857 (2023).
28. Meredith, S. D., Zuback, J. S., Keist, J. S. & Palmer, T. A. Impact of composition on the heat treatment response of additively manufactured 17–4 PH grade stainless steel. *Materials Science and Engineering A* **738**, 44–56 (2018).
29. Facchini, L. *et al.* Metastable Austenite in 17–4 Precipitation-Hardening Stainless Steel Produced by Selective Laser Melting. *Advanced Engineering Materials* **12**, 184–188 (2010).
30. Yadollahi, A., Shamsaei, N., Thompson, S. M., Elwany, A. & Bian, L. Effects of building orientation and heat treatment on fatigue behavior of selective laser melted 17-4 PH stainless steel. *International Journal of Fatigue* **94**, 218–235 (2017).
31. LeBrun, T., Nakamoto, T., Horikawa, K. & Kobayashi, H. Effect of retained austenite on subsequent thermal processing and resultant mechanical properties of selective laser melted 17–4 PH stainless steel. *Materials & Design* **81**, 44–53 (2015).
32. Sun, Y., Hebert, R. J. & Aindow, M. Effect of heat treatments on microstructural evolution of additively manufactured and wrought 17-4PH stainless steel. *Materials & Design* **156**, 429–440 (2018).
33. Sabooni, S. *et al.* Laser powder bed fusion of 17–4 PH stainless steel: A comparative study on the effect of heat treatment on the microstructure evolution and mechanical properties. *Additive Manufacturing* **46**, 102176 (2021).

34. Alnajjar, M., Christien, F., Wolski, K. & Bosch, C. Evidence of austenite by-passing in a stainless steel obtained from laser melting additive manufacturing. *Additive Manufacturing* **25**, 187–195 (2019).

35. Chattopadhyay, C., Sangal, S. & Mondal, K. A relook at the preferred growth direction of the solid–liquid interface during solidification of pure metals. *Acta Materialia* **58**, 5342–5353 (2010).

36. Tang, S. *et al.* Orientation selection process during the early stage of cubic dendrite growth: A phase-field crystal study. *Acta Materialia* **60**, 5501–5507 (2012).

37. Boukellal, A. K. *et al.* Grain growth competition and formation of grain boundaries during solidification of hcp alloys. *Acta Materialia* **269**, 119830 (2024).

38. DebRoy, T. *et al.* Additive manufacturing of metallic components – Process, structure and properties. *Progress in Materials Science* **92**, 112–224 (2018).

39. Dinda, G. P., Dasgupta, A. K. & Mazumder, J. Texture control during laser deposition of nickel-based superalloy. *Scripta Materialia* **67**, 503–506 (2012).

40. Vysotskiy, I., Malopheyev, S., Zuiko, I., Mironov, S. & Kaibyshev, R. Crystallographic aspects of 17–4 PH martensitic steel produced by laser-powder bed fusion. *Materials Characterization* **194**, 112405 (2022).

41. Weld Metal Solidification I: Grain Structure. in *Welding Metallurgy* 170–198 (John Wiley & Sons, Ltd, 2002). doi:10.1002/0471434027.ch7.

42. Bustillos, J. *et al.* Alloy amalgamation: Unlocking the co-existence of multiple phases in additively manufactured titanium alloys. *Applied Materials Today* **42**, 102606 (2025).

43. Wakai, A. *et al.* Harnessing metastability for grain size control in multiprincipal element alloys during additive manufacturing. *Nat Commun* **16**, 1446 (2025).

44. Dass, A., Gabourel, A., Pagan, D. & Moridi, A. Laser based directed energy deposition system for operando synchrotron x-ray experiments. *Rev. Sci. Instrum.* **93**, 075106 (2022).

45. Toby, B. H. & Von Dreele, R. B. GSAS-II: the genesis of a modern open-source all purpose crystallography software package. *Journal of Applied Crystallography* **46**, 544–549 (2013).

46. Hielscher, R., Silbermann, C. B., Schmidl, E. & Ihlemann, J. Denoising of crystal orientation maps. *J Appl Cryst* **52**, 984–996 (2019).

47. Atreya, V., Bos, C. & Santofimia, M. J. Understanding ferrite deformation caused by austenite to martensite transformation in dual phase steels. *Scripta Materialia* **202**, 114032 (2021).

48. Hossain, R., Pahlevani, F., Quadir, M. Z. & Sahajwalla, V. Stability of retained austenite in high carbon steel under compressive stress: an investigation from macro to nano scale. *Sci Rep* **6**, 34958 (2016).

49. Liu, T.-W. & Wu, X.-L. Martensitic transformation pathways and crystallographic orientation relationships in steel. *Journal of Materials Science & Technology* **174**, 74–84 (2024).

50. Martinez Ostormujof, T. *et al.* Deep Learning for automated phase segmentation in EBSD maps. A case study in Dual Phase steel microstructures. *Materials Characterization* **184**, 111638 (2022).

51. Breumier, S. *et al.* Leveraging EBSD data by deep learning for bainite, ferrite and martensite segmentation. *Materials Characterization* **186**, 111805 (2022).

52. Kang, S. H. *et al.* A Quantitative Evaluation of Microstructure by Electron Back-Scattered Diffraction Pattern Quality Variations. *Microanal* **19**, 83–88 (2013).

53. Calcagnotto, M., Ponge, D., Demir, E. & Raabe, D. Orientation gradients and geometrically necessary dislocations in ultrafine grained dual-phase steels studied by 2D and 3D EBSD. *Materials Science and Engineering: A* **527**, 2738–2746 (2010).

54. Elmer, J. W., Allen, S. M. & Eagar, T. W. Microstructural development during solidification of stainless steel alloys. *Metall Trans A* **20**, 2117–2131 (1989).

Supplementary Files

This is a list of supplementary files associated with this preprint. Click to download.

- PH174AdvMatSIfinal.docx